

Application No. 09/869,638  
Filed: February 8, 2002  
TC Art Unit: 2621  
Confirmation No.: 5891

REMARKS

Pending claims 1-3, 6-12 and 14 have been rejected as obvious over Luck et al. in view of Diouf et al. [sic, Watkin] and Watanabe. Claims 4, 5, 13 and 15 have been rejected as obvious over Luck et al., in view of Diouf et al. and Watanabe, and further in view of Hemstreet, III et al. These rejections are respectfully traversed for the reasons given below and reconsideration is requested.

The present invention is directed to a method for the automatic analysis of microscope images of biological objects, which is particularly useful for the analysis of fluorescence images of cells. In making the rejection, the Examiner has characterized the disclosure of the primary reference, Luck et al., in relation to the various steps of Applicants' method claim 1. In making this characterization, however, the Examiner has made numerous misinterpretations of Luck et al.

For, example, in reference to step b) of Applicants' claim 1, the Examiner cites to col. 7, lines 46-53 and col. 13, lines 17-23, of Luck et al. for comparison. The Examiner appears to have centered on the word "training" and assumed that all training of a neural network is equal. However, this is not the case. It is the specific method of training the neural network and the application of that trained network to actual samples that produce the advantages coming from use of the method of the invention.

In the method of the invention, training is based on selecting a first microscope image, using a number n of first image excerpts constituting a positive training set, the first image excerpts comprising the position of mass gravity centers of individual objects in the first microscopic image, and selecting

Application No. 09/869,638  
Filed: February 8, 2002  
TC Art Unit: 2621  
Confirmation No.: 5891

and marking a number  $m$  of second image excerpts ("in the same first microscope image"), each spaced a predetermined minimal distance from the first image excerpt (so that they will be away from individual objects), the number  $m$  of such marked second image excerpts constituting a negative training set. Then, training is made as follows: characteristic features (and/or feature combinations) of the positive and negative training sets are determined, and a classification value between 0 and 1 is given to each on the basis of the positive training set being assigned the value 1 and the negative training set being assigned the value 0.

For all further microscope images in the method of the invention, the system trained on the first image is then applied. Classification values are determined and the recognition of the position of biological objects in these further images, step f), is based on a threshold criterion with respect to the classification values. Thus, in summary, the method of the invention is directed to automatic analysis of microscope images including training on a first image and recognition of the position(s) of biological objects in subsequent images following the training.

In contrast, Luck et al. discloses classifying cells based on their morphology and not by recognition of their position(s). According to Luck et al., a "primary" classification is carried out on images that have been found based on two scans. The first scan, at low resolution, is used to determine those areas of a slide that contain at least a portion of a specimen. A high resolution scan is then conducted on those determined portions, and the primary classification to find the centroids of biological objects having desired attributes is carried out (col. 3, line 55

Application No. 09/869,638  
Filed: February 8, 2002  
TC Art Unit: 2621  
Confirmation No.: 5891

- col. 4, line 19). Then, based on previously performed training, which is not described, with a training set of "several hundred or thousands of known benign and premalignant cells," the secondary classification is carried out to determine the the likelihood that the object is a specific type of cell (col. 13, lines 12-23). Thus, Luck et al. does not disclose an interrelationship between training, as recited in steps b) - d) of Applicants' claim 1, and use of the results of the training on second and subsequent microscopic images, as required by step d) of Aplicants' claim 1.

That the Examiner has mixed up several issues in Luck et al. in order to find some correspondence to the wording of Applicant's claim 1 is made more evident by the fact that steps c) and f) of the method according to claim 1 are not explicitly mentioned in the Examiner's analysis of the disclosure of Luck et al. In regard to the contents of Applicants' step c), the Examiner states that the "complete training set consists of a positive (1) and a negative (0) training set" and makes reference to col. 13, lines 40-48 of Luck et al. However, as described above, Luck et al. does not disclose two separate training sets determined on the same image, as required by Applicants' claim 1.

Further, regarding item c), the Examiner argues:

Luck does not disclose using minimum distance for classification purposes. Computing distance for classifying images is extremely well-known as evidenced by Diouf et al. [sic, Watkin] see third paragraph on page 529.

Therefore, it would have been obvious to one having ordinary skill in the art at the time of the invention to use a minimal distance for classification in the medical field (as disclosed by Diouf et al. [sic, Watkin]) in the method disclosed by Luck for no other reason than to classify the medical images correctly.

Application No. 09/869,638  
Filed: February 8, 2002  
TC Art Unit: 2621  
Confirmation No.: 5891

The Applicants submit that combining Diouf et al. with Luck et al. is merely impermissible hindsight reconstruction on the basis of the Applicants' claims. Furthermore, even a combination of these references would not result in the teachings stated by the Examiner.

Diouf et al., at p. 25, third paragraph, discloses a formula providing a statistic that is dependent on the minimum of distance  $d$  wherein  $d$  is defined to be  $R' - m_i'$ , and wherein  $R'$  is random vector (see explanation of formula (7) in the right hand column of p. 528), and wherein  $m_i$  is the expected value of a random variable (see once again p. 528, at the bottom). The distance referenced at that cite does not have anything to do with image excerpts. In fact, Diouf et al. does not do more than mention the words "minimum distance." It appears that this reference has been found as result of a key word search including "minimum" and "distance."

The Examiner then looks to Watanabe to obtain the other acknowledged "missing piece" from Luck et al., that the reference "does not disclose using 1 and 0 for training a neural network." Watanabe, however, does not do anything more than to briefly mention values of 0 and 1 for the same variable (col. 5, lines 59-61) in the context of a "neuralnetwork and learning method." Applicants explicitly point out that the cited text passage in Watanabe relates to the same variable  $y$ , which can have two different values. It is clearly based on a hindsight approach for the Examiner to use Watanabe in this manner. In addition, even if the references are combined, the combined disclosures still would not teach all the elements of the Applicants' claim 1, as recited above.

Application No. 09/869,638  
Filed: February 8, 2002  
TC Art Unit: 2621  
Confirmation No.: 5891

Finally, the Examiner makes no assertion that the combination of the cited references would even result in teaching Applicants' step f) and, thus, the Examiner does not even make a *prima facie* case for an obviousness rejection of the invention as particularly claimed by the Applicants.

Thus, the Applicants submit that the rejection of claim 1 as obvious over Luck et al. in view of Diouf et al. and Watanabe has been overcome. The Examiner has, furthermore, rejected dependent claims 2, 3, 6-12 and 14 as obvious over these cited references. The Examiner submits that the indicated claims are allowable for being dependent on an allowable base claim, as discussed above. In regard to dependent claims 4, 5, 13 and 15, the Examiner has rejected them as obvious over the previously cited references and further in view of Hemstreet, III et al. The Applicants submit that the Hemstreet, III et al. disclosure in no way supplies the deficiencies in the primary references, as recited above, and, therefore, this rejection, too, has been overcome.

Thus, the Applicants submit that all claims are in condition for allowance and such action is respectfully requested.

For the Examiner's information, the Applicants have attached herewith two journal articles, published after the filing of the instant application, which describe practice of the method of the invention.

Application No. 09/869,638  
Filed: February 8, 2002  
TC Art Unit: 2621  
Confirmation No.: 5891

The Examiner is encouraged to telephone the undersigned attorney to discuss any matter that would expedite allowance of the present application.

Respectfully submitted,

TIM WILHELM NATTKEMPER ET AL.

By: Holliday C. Heine  
Holliday C. Heine, Ph.D.  
Registration No. 34,346  
Attorney for Applicant(s)

WEINGARTEN, SCHURGIN,  
GAGNERIN & LEBOVICI LLP  
Ten Post Office Square  
Boston, MA 02109  
Telephone: (617) 542-2290  
Telecopier: (617) 451-0313

HCH/raw  
324802-1

-11-

WEINGARTEN, SCHURGIN,  
GAGNERIN & LEBOVICI LLP  
TEL. (617) 542-2290

PAGE 13/36 \* RCVD AT 8/5/2005 3:19:19 PM [Eastern Daylight Time] \* SVR:USPTO-EXRF-6/26 \* DNIS:2738300 \* CSID:6176950892 \* DURATION (mm:ss):11-14

## INTRODUCTION

# A Neural Classifier Enabling High-Throughput Topological Analysis of Lymphocytes in Tissue Sections

Tim W. Nattkemper<sup>1</sup>, Helge Ritter<sup>2</sup>, Walter Schubert<sup>1,3</sup>

**Abstract**—A neural cell detection system (NCDS) for the automatic quantitation of fluorescent lymphocytes in tissue sections is presented. The system acquires visual knowledge from a set of training cell-image patches selected by a user. The trained system evaluates an image in two minutes calculating (i) the number, (ii) the positions, and (iii) the phenotypes of the fluorescent cells. For validation, the NCDS learning performance was tested by cross validation on digitized images of tissue sections obtained from inherently different types of tissue: diagnostic tissue sections across the human tonsil and across an inflammatory lymphocyte infiltrate of the human skeletal muscle. The NCDS detection results were compared with detection results from biomedical experts and were visually evaluated by our most experienced biomedical expert. Although the micrographs were noisy and the fluorescent cells varied in shape and size, the NCDS detected a minimum of 95% of the cells. In contrast, the cellular counts based on visual cell recognition of the experts were inconsistent and largely unreproducible for approx. 80% of the lymphocytes present in a visual field. The data indicate that the NCDS is rapid and delivers highly reproducible results, and therefore enables high-throughput topological screening of lymphocytes in many types of tissue, as for example obtained by routine diagnostic biopsy procedures. High-throughput screening with the NCDS provides the platform for the quantitative analysis of the interrelationship between tissue environment, cellular phenotype and cellular topology.

**Keywords**—Shape recognition, Object detection, Fluorescence Microscopy, Functional Proteomics

## INTRODUCTION

High throughput screening (HTS) of lymphocytes in liquids samples by flow cytometry has been known for years as a powerful technique for rapid and homogeneous measurements of many cellular parameters. The technique has been successfully used to identify a large number of lymphocyte phenotypes in the blood and analyze their functions. These studies are performed by the application of mono-clonal antibodies (mAbs) directed against cell surface antigens, referred to as the cluster of differentiation (CD) antigens. Flow cytometric HTS has provided important insight into immunoregulatory events at the cellular level of circulating immune cells in many diseases, such as the autoimmune disorders, the immunodeficiency syndromes, and malignancies, and has led to numerous applications in diagnostic and therapeutic strategies ([1],[2],[3],[4]). Many important aspects of the cellular immune system, however, are reflected by the ability of lymphocytes for homing and invasion of different organ systems, where these cells organize themselves as dense lymphoid tissue, or simply migrate as single cells. This implies that the tissue specific functional organization of the lymphocytes that have escaped the circulation must be analyzed at their correct anatomical sites. In contrast to the flow cytometric measurements of lymphocytes in the blood or other liquids, the analysis of lymphocytes in tissue sections has remained restricted to visual evaluation in various types of microscopes for years.

The objective of this study is to introduce and validate a rapid learning algorithm enabling automatic lymphocyte recognition and quantitative analysis on the basis of digitized fluorescent images. The approach enables routine HTS of lymphocytes at their correct anatomical sites. By its complementarity to flow cytometric screening of lymphocytes in body liquids, our algorithm now allows the assessment of the functional organization of the lymphocytes in solid tissues by a highly standardized HTS procedure.

<sup>1</sup>Neuroinformatics Group, University of Bielefeld, E-mail: nattkem@techfak.uni-bielefeld.de

<sup>2</sup>Neuroimmunology and Molecular Pattern Recognition Group, University of Magdeburg,

<sup>3</sup>MELTEC Ltd., E-mail: schubert@pc.meltec.de

Nattkemper et al.,  
IEEE Trans. on Inf. Techn. in

Biomed., Vol. 5, No. 2  
pp. 138-149, June 2001

to appear in *IEEE Trans. on Information Technology in Biomedicine*

Lymphocytes constitute an important fraction of the cellular immune system. Besides their physiological role in immunosurveillance and defence of infections, the lymphocytes play an essential part in many diseases, because they can invade and progressively destroy organs. For example, relapsing lymphocyte infiltration of target organs is the hallmark of the autoimmune diseases, and nearly any organ can be the target for lymphocyte infiltration. Besides autoimmune diseases, lymphocyte infiltration is the proximal cause of the rejection of transplanted organs, and lymphocyte invasion of the artery wall is an early, probably primary event in the pathogenesis of atherosclerosis [5]. Together these clinical syndromes constitute the major fraction of the diseases in the western world.

In the case of infiltration of organs leading to chronic inflammation, it is a frequent routine procedure in clinical practice to assess a precise diagnosis on the basis of biopsies. Biopsies can easily be taken from nearly any organ system. Microscopic evaluation of lymphocytes in these clinical samples is a standard procedure in pathology laboratories. The classification of a lymphocyte infiltrate in biopsy tissue sections has been largely restricted to visual microscopic analysis by medical experts. Usually lymphocytes in tissue sections are stained for one given surface antigen visualized by, for example, immunoperoxidase reaction. Given many serial sections of a tissue site each stained for a different antigen, medical experts acquire rapidly a semi-quantitative result concerning i) the type of lymphocytes present in the tissue and ii) the distribution of this type. However, many different parameters of each single lymphocyte must be evaluated simultaneously. Correlating locally corresponding signals of fluorescent lymphocytes can not be done by simple visual inspection. Hence intercellular functional correlations of higher order remain hidden in the image data.

For the latter purpose cell detection has to satisfy four main requirements: First, one microscope image has to be evaluated in a very short time to enable high throughput in screening many tissue sections. Second, results must be reproducible to guarantee a reasonable statistical interpretation of the data. Third, a good detection performance by good generalization is a requirement because cells vary in shape, density and fluorescence properties. Fourth, microscope images may be taken at different magnifications so that the detection system must be easy to adapt to changes of the cells' pixel size by a non-expert user.

Detection algorithms in related applications are based

on the ideas of fitting a model to a gradient ensemble ([6], [7]), wave propagation [8], boundary tracing [9] or use the Hough-transform ([10],[11]) to detect circle-like objects. In our present study the objects considered are lymphocytes during a migration in tissue, so their shapes show considerable variation. Furthermore we use immunofluorescence labeling of these lymphocytes. The resulting images are noisy because of heterogenous signals reflecting different concentrations of cell surface proteins which were labeled by an antibody conjugated to a fluorescent dye. These factors make it difficult to define a model fitting for all cells in the image. Thus, many of the above approaches seem unsuitable for our scenario.

In this paper we present the Neural Cell Detection System (NCDS) which uses an adaptive neural classifier, mapping each image point  $p$  in a fluorescence micrograph to an evidence value  $C(p) \in [0; 1]$ . The magnitude of the evidence value estimates the probability for the image point to be occupied by a fluorescent cell. A local maximum search in the evidences of all image points combined with a thresholding procedure then can deliver the desired positions of fluorescent cells.

The classifier is a special kind of an artificial neural net which has been shown to be very efficient in fast learning of non-linear classification tasks from even small training sets. In this work, the training set consists of image patches from one fluorescence image. One subset of it contains positive cell classification examples. These are obtained with the help of a human expert who is experienced in analyzing fluorescence micrographs. The expert identifies in the training image with a mouse pointer all these locations where he judges a cell to be present. The other subset contains negative cell classification examples. Images from this subset are randomly chosen patches from cell-free regions. The purpose of these images is to adapt the classifier to the typical background structures that are present in the microscope images and that must be rejected by the classifier to obtain good performance. The training of the neural classifier and the following cell detection in a set of fluorescence images is done automatically without user interaction. Thereby we reduce the required user interaction for adapting the NCDS to the selection of positive and negative examples in a training set for the neural classifier.

For system validation of the NCDS the learning and classification performance was analyzed. The most important property of a neural classifier is its classification performance on new data after training. To

BEST AVAILABLE COPY.

to appear in IEEE Trans. on Information Technology in Biomedicine

measure the error rate of the latter we use cross-validation. In addition, the cells, which were detected in images by the NCDS were compared with detection results of five human experts who marked the fluorescent cells manually and independently from each other. The resulting five expert lists of cell positions were analyzed concerning the validity of these lists for calculating error rates. Additionally, the error rates of the NCDS were estimated by one expert by visual inspection of its detection result. This expert has a most outstanding experience in the visual analysis of fluorescence micrographs and is referred to as expert A in the following.

## II. MATERIAL

The objects for our cell recognition approach were fluorescently labeled lymphocytes in tissue sections. The sections were obtained from various human tissues. Our analysis was focused on lymphocytes having invaded muscle tissue during disease (human sarcoid myopathy), and on lymphocytes forming dense clusters within the tonsil. The tissue sections were processed for immunofluorescence labeling with mAbs against cell surface antigens as described in [12] and [13]. We used a standardized protocol for the preparation of frozen tissues according to a) thickness of cryostat sections ( $4 \mu m$ ) and b) incubation with antibodies (concentration:  $1 \frac{mg}{ml}$  buffer ([12],[13])). To label cell surfaces of lymphocytes *in situ*, we have chosen mAbs against the receptors belonging to the cluster of differentiation antigens (CD). Here we have labeled the CD4 and the CD3 antigens as characteristic. Visual fields within the labeled tissue sections were selected by a medical expert. The fluorescence signals of FITC (Fluorescein-iso-thio-cyanate) conjugated to the mAbs were visualized in a standard fluorescence microscope (ZEISS Axiophot) equipped with a HBO-50 vapor lamp and a cooled CCD-camera (Photometrics MAC 300). Images were digitized under standard conditions including a) time for signal recording after excitation, and b) use of optical parameters (objective 16 $\times$ , 40 $\times$ , filter set BP 415/FT 510/BP 515-545 nm; Optivar factor 1.25). The digitized images were not post-processed.

Figure 1 gives a characteristic example of lymphocytes of an inflammatory infiltrate in the human muscle tissue, fluorescently labeled for the CD4 cell surface antigen.

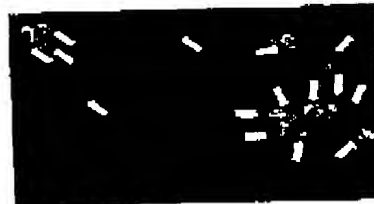


Fig. 1. Fluorescence micrograph illustrating CD4-immunolabeled invasive lymphocytes in muscle tissue. The white arrows point at some fluorescent lymphocytes as examples of many others present in the site. The cells vary in contrast, shape, and size which is characteristic for cells in organ tissue structures.

## III. METHODS

In this chapter we describe the training and the application of the NCDS and the methods used for system validation, including comparison with cell recognition efficiency of five experts (termed A,B,C,D,E).

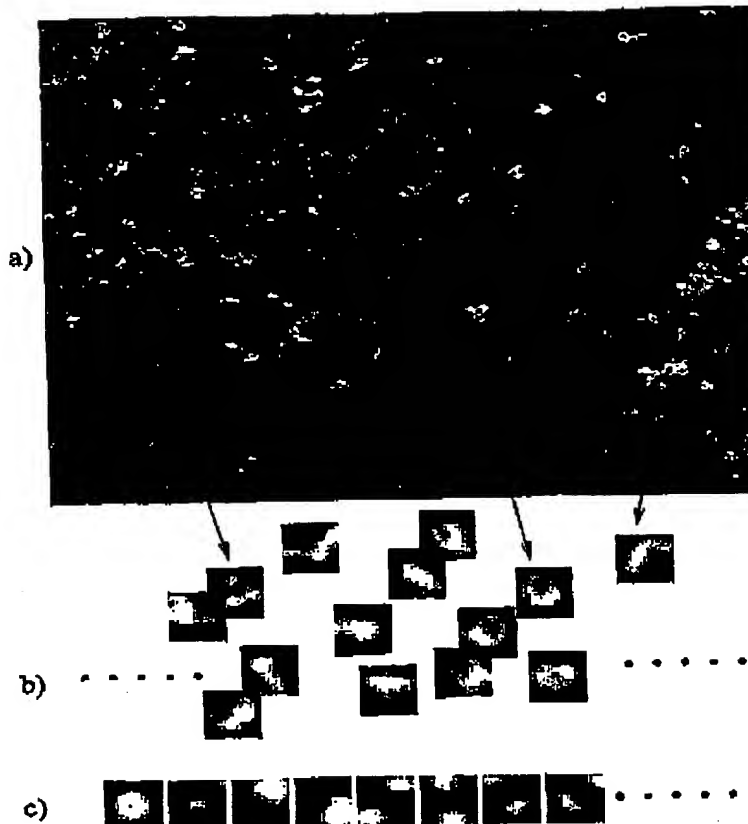
### A. The Training Set

To train the neural classifier a training set  $\Gamma$  of  $M$  (input,output)-pairs

$$\Gamma = \{(x_\alpha, y_\alpha)\}, \alpha = 1 \dots M$$

is created. The set is composed of two subsets  $\Gamma = \Gamma^{pos} \cup \Gamma^{neg}$ . The positive set  $\Gamma^{pos} = \{(x_\alpha^{pos}, 1)\}$  consists of feature vectors  $x_\alpha^{pos}$  computed (see B. below) from image patches centered at positive training samples for fluorescent cells, together with the target output value  $y_\alpha^{pos} = 1$  of the classifier. The other set  $\Gamma^{neg} = \{(x_\alpha^{neg}, 0)\}$  consists of feature vectors  $x_\alpha^{neg}$  computed from non-cell image patches (cf. B below) and their target classification output value  $y_\alpha^{neg} = 0$ . The image patches for computing the feature vectors  $x_\alpha^{pos} \in \Gamma^{pos}$  are obtained with the aid of an interactive program that displays the digitized microscope images and allows a user to select cell centers with the aid of a mouse cursor. The set  $\Gamma^{neg}$  is then generated automatically by randomly selecting image points in a minimum distance of  $r_{neg}$  pixels from any of the selected cells of  $\Gamma^{pos}$ . In this work we set  $r_{neg} = 5$ . Small changes of this parameter affect the system performance only marginally. For each of these randomly selected points a feature vector  $x_\alpha^{neg}$  is computed by the same procedure as for  $\Gamma^{pos}$ .

to appear in IEEE Trans. on Information Technology in Biomedicine



BEST AVAILABLE COPY

Fig. 2. a) Fluorescence micrograph illustrating muscle invasive lymphocytes labeled for CD4 antigen at the cell surface. b) Enlarged cross-sectioned lymphocytes demonstrating their cellular shape variation. c) Eigencells calculated from manual mouse-click selection of 120 cross-sectioned lymphocytes.

### B. Calculation of Feature Vectors

Choosing suitable features is crucial for the performance of a classification system. In the context of our work the features should be robust against small changes of size, intensity and curvature of the fluorescent cells in the patches (see figure 2). Furthermore, they should guarantee a good separation between cells and non-cells in the  $d_m$ -dimensional feature space. One way to map an image point  $p$  to a feature vector  $x \in \mathbb{R}^{d_m}$  is to calculate the overlaps of a surrounding image region of size  $N \times N$  with a set of  $d_m$  filters. Such filters can be a set of tuned Gabor filters ([14],[15]) or steerable derivatives of 2-dimensional Gaussians [16]. One disadvantage of these methods is that they contain several parameters (radius, orientations, etc.) which have to be fit-

ted according to the particular application. Handling of this problem is difficult and time-consuming for a non-expert user. We use here a data-driven approach, a Principal Component Analysis (PCA) on a set of  $N \times N$ -sized image patches of centered cells. The PCA-technique uses  $d_m$  eigenvectors  $u_\lambda \in \mathbb{R}^{N^2}$  (so called "eigencells") of the covariance matrix of  $N \times N$  image patches. The patches are the  $N \times N$ -sized image regions around the hand-selected image points of fluorescent cells. Figure 2 gives a set of patches (2b) with the eigencells corresponding to the highest eigenvalues (2c). The usage of such eigenvectors is a well-known technique for detection tasks ([17],[18]). A listing of the eigenvalues in descending order reveals that majority of the variance in the image data is described by the six eigencells of the six highest eigenvalues. These are taken to generate the

to appear in IEEE Trans. on Information Technology in Biomedicine

6-dimensional feature vector  $\mathbf{x}$  for an image point by scalar multiplication of its  $N \times N$  neighborhood with the six eigencells.

### C. The Neural Classifier

We use an artificial neural net of Local Linear Map-type (LLM) for classification. The LLM was introduced in [19] and has been shown to be a powerful tool for the fast learning of non-linear mappings

$$C: \mathbb{R}^{d_{in}} \mapsto \mathbb{R}^{d_{out}},$$

such as classification tasks in Computer Vision applications [20]. The LLM-approach was originally motivated by the Kohonen Self-organizing Map ([21],[22]) with the aim to obtain a good map resolution even with a small number of units. Recently, there have been a number of proposals for algorithms with the same objective, but a somewhat different mathematical basis. The GTM-approach [23] creates a map manifold on the basis of a statistical estimation procedure (maximum likelihood approach). While the authors argue that their method, therefore, is "more principled" as compared to the standard SOM, it is at the same time also computationally heavier and more complex to implement. Another proposal is by [24], which is rather attractive due to its high computational efficiency. Other proposals, such as [25], combine the SOM with the (computationally also much more expensive) Sammon Map [26], using subsampling strategies and MLP-based interpolation schemes to arrive at a computationally efficient method. Since we here are primarily interested in classification, the present application is unlikely to benefit much from the modifications proposed in the cited references. For a quantitative comparison with some more standard approaches, see e.g. [27]. A collection of recent applications of the SOM can be found in [28].

In the present paper the dimensions are  $d_{in} = 6$  and  $d_{out} = 1$ . In the following the algorithm is described in general. The LLM combines unsupervised and supervised learning in contrast to the widely used multi-layer perceptron trained with back-propagation [29]. The LLM is given through

$$\{w_i^{in} \in \mathbb{R}^{d_{in}}, w_i^{out} \in \mathbb{R}^{d_{out}}, A_i \in \mathbb{R}^{d_{in} \times d_{out}}, i = 1..n\}.$$

We call a triple  $v_i = (w_i^{in}, w_i^{out}, A_i)$  a node. Once the LLM is trained an input vector  $\mathbf{x}$  is mapped to an output  $C(\mathbf{x})$  by calculating

$$C(\mathbf{x}) = w_i^{out} + A_i(\mathbf{x} - w_i^{in})$$

with  $\kappa = \arg \min_i \|\mathbf{x} - w_i^{in}\|$ . So  $w_i^{in}$  is the nearest neighbor to input  $\mathbf{x}$ . The mapping into the output space is performed by a local linear transformation given by  $A_\kappa$  and  $w_\kappa^{out}$ . An illustration is given in figure 3.

To train the three free parameters of each of the  $n$  nodes ( $w_i^{in}, w_i^{out}, A_i, i = 1..n$ ) we (i) select input-output pairs  $(\mathbf{x}_a, y_a)$  from the training set  $\Gamma = \{(\mathbf{x}_a, y_a)\}$ , (ii) find for each the best-match node  $\kappa$ , and (iii) change its weights according to the learning rules

$$\Delta w_\kappa^{in} = \epsilon^{in}(\mathbf{x}_a - w_\kappa^{in}) \quad (1)$$

$$\Delta w_\kappa^{out} = \epsilon^{out}(y_a - C(\mathbf{x}_a)) + A_\kappa \Delta w_\kappa^{in} \quad (2)$$

$$\Delta A_\kappa = \epsilon^A(y_a - C(\mathbf{x}_a)) \frac{(\mathbf{x}_a - w_\kappa^{in})^T}{\|\mathbf{x}_a - w_\kappa^{in}\|^2} \quad (3)$$

with  $\epsilon^{in}, \epsilon^{out}, \epsilon^A \in [0, 1]$  as learning step sizes. Looking at the rules, one can observe that learning rule (1) is the online version of k-means [30] for positioning the  $n$  centers of  $w_i^{in}$  (see figure 4). The learning rules (2) and (3) are for the adjustment of a linear mapping specified by vector  $w_i^{out}$  and matrix  $A_\kappa$  in the vicinity (Voronoi cell) around the best match node.

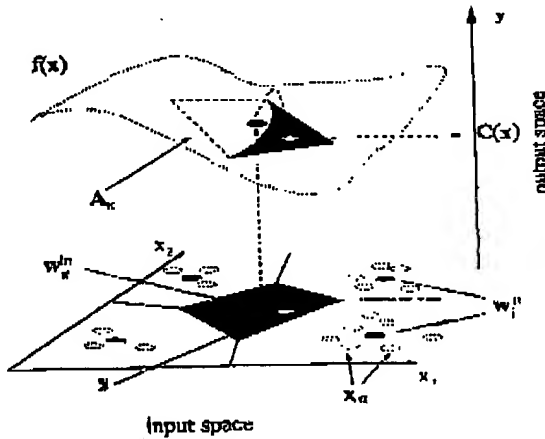


Fig. 3. Example illustrating a Local Linear Map approximating a function  $f(\mathbf{x}), \mathbf{x} \in \mathbb{R}^3$  (dotted plane) with five nodes. The LLM's nodes'  $w_i^{in}$  form Voronoi cells of the input space. The plane is approximated by projections of the cells (one sketched as dark grey plane). An input vector  $\mathbf{x}$  is mapped to  $C(\mathbf{x})$  in the output space. First, the nearest neighbor  $w_\kappa^{in}$  to the input is selected, then the input is mapped via the coupled matrix  $A_\kappa$  (dashed arrows).

to appear in *IEEE Trans. on Information Technology in Biomedicine*

#### D. Automatic Cell Detection

To calculate the desired positions of the fluorescent cells in an image every image point  $p$  is mapped to its evidence value  $[0; 1]$  by calculating the feature vector  $x$  of its surrounding  $N \times N$ -image patch and its LLM output  $C(x) \in [0, 1]$ . The output is the evidence value for a fluorescent lymphocyte at position  $p$ . By mapping all the evidences to their corresponding image positions we achieve a so called *evidence map*. A point  $p$  in the evidence map which has the highest evidence value  $C(x)$  within a  $\frac{N}{2}$  radius above a given threshold is the result position of the center of a fluorescent cell, if  $C(x)$  obeys

$$C(p) > 0.5 \wedge C(p) = \arg \max_{d(p,p') < \frac{N}{2}} \{C(p')\}.$$

#### E. Optimized Learning with Activity Equalization Vector Quantization

One problem of a winner-take-all vector quantization in equation (1) of the learning rules is that the input feature space may not be approximated efficiently. The reason is that a fraction of the randomly initialized  $w_i^{in}$  can become stuck in regions of the input feature space, containing none of the  $x_\alpha$ . To achieve a better quantization of the input space an extension is made to the LLM learning scheme, the so called *Activity Equalization Vector Quantization (AEV)* which

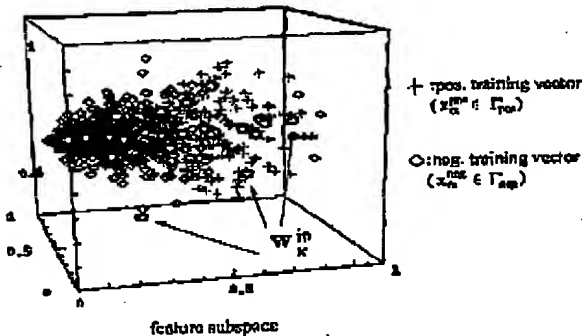


Fig. 4. The first three components of the 6-dimensional training vectors  $x_\alpha$  are plotted with an AEV quantization by 25 reference vectors  $w_i^{in}$  (grey-dark grey bullets) for example. One can observe that the cell features (grey plus-symbol) and the non-cell features (black diamond) form two overlapping clusters. The other three components the components have a similar distribution. All 25 nodes contribute to the approximation of the feature distribution to the same amount and a good approximation of the distribution is achieved.

was introduced and discussed in [31] and [32]. After an epoch of  $T$  learning steps for each node we evaluate its activity. The activity of a node is defined as how often the node was the nearest node to a training input. We define the average activity  $a_i$  of the  $i$ -th node within a sweep of  $T$  learning steps as  $a_i = \frac{1}{T} \sum_t h(w_i^{in}, x(t))$  with

$$h(w_i^{in}, x(t)) = \begin{cases} 1 & \text{if } w_i^{in} \text{ is the nearest neighbour} \\ & \text{to the input } x(t) \text{ at training} \\ & \text{step } t \in [1 \dots T], \\ 0 & \text{else} \end{cases}$$

$x(t)$  denotes the training input of the  $t$ -th training step of a period of  $T$  steps. The basic idea of the AEV is that after each  $T$  learning steps the activities of the nodes are computed and a set

$$I = \{i | a_i < \theta\}$$

of "inactive nodes" (i.e., nodes whose average activity is below a chosen threshold  $\theta$ ) is determined. A randomly chosen fraction  $f$  of nodes in  $I$  is then repositioned by shifting them by a minimal distance  $r_{capl}$  in a random direction, i.e. the new node has to obey

$$\|w_i^{in,new} - w_i^{in}\| > r_{capl}.$$

The rationale behind this is to ensure a better exploration of the input space.

The remaining fraction  $1 - f$  of nodes in  $I$  is repositioned to random locations in the neighborhood of active nodes

$$J = \{j | a_j \geq \theta\}.$$

I. e., the new positions  $w_i^{in,new}$  of these nodes have to obey

$$\|w_i^{in,new} - w_j^{in}\| < r_{sc}.$$

The rationale behind these moves is to ensure a better activity equalization among nodes and to better populate densely clustered areas in the input space. For the application of the AEV the  $T_{learn}$  learning steps are divided into three intervals  $[1, \dots, T_1]$ ,  $[T_1 + 1, \dots, T_2]$  and  $[T_2 + 1, \dots, T_{learn}]$ . In the first phase after every  $T$  learning steps the activities of the nodes are computed and  $f$  is chosen as  $f = 0.5$ . After the first phase the exploration is finished and in the second phase we chose  $f = 0.0$ , i.e. reposition nodes only. In the third phase the AEV is finished and the LLM is trained by applying learning rules (1)-(3). In this application the LLM is trained in  $T_{learn} =$

to appear in *IEEE Trans. on Information Technology in Biomedicine*

$n * 10^6$  steps. The interval borders were set to  $T_1 = 0.2 * T_{learn}$  and  $T_2 = 0.4 * T_{learn}$ . The length of a period  $T$  was set to  $T = n * 100$ .

#### F. System Validation

For system validation the performance of the NCDS was analyzed concerning two aspects. First, the learning and generalization performance of the LLM was analyzed by cross validation [33]. To perform a cross validation the data set  $\Gamma$  that we use for our evaluation is divided into six disjoint subsets  $\Gamma = \bigcup_i \Gamma_i, i = 1, \dots, 6$  each of equal size, containing the same numbers of positive and negative training samples. Five of the subsets form the training set  $\Gamma_{train}$  and the sixth is the test set  $\Gamma_{test}$ . After the NCDS has been trained on  $\Gamma_{train}$  the inputs from  $\Gamma_{test}$  are classified to evidence values by the LLM. Because the test data consists of feature vectors computed for single image patches, only the classification performance of the LLM on the feature vectors is evaluated. So only the evidence values calculated for the feature vectors of  $\Gamma_{test}$  are considered here. If the evidence value  $C(x_\alpha), x_\alpha \in \Gamma_{test}$ , is larger than 0.5 the patch is classified as a cell, otherwise it is rejected. Thereby a classification rate for the test samples of  $\Gamma_{test}$  was calculated for the positive samples  $\Gamma_{test}^{\text{pos}}$  and for the negative ones,  $\Gamma_{test}^{\text{neg}}$ . We then repeat the entire procedure five more times with each  $\Gamma_i$  selected as  $\Gamma_{test}$ . Classification rates on negative and positive examples are calculated separately. The rates give a good approximation about the classifiers ability not only to learn the training set but also to classify new input data correctly.

The second aspect of validation is to apply the NCDS to the images, and then measure error rates for the detected positions of fluorescent cells by Receiver Operator Characteristic (ROC) measures (see [34] for a review). One error measurement was done by visual inspection of the NCDS-detected cells by our most experienced expert A. In addition, the NCDS detection result was also compared with the results of cell detection, carried out by human individuals. For this purpose one preselected micrograph was evaluated by the NCDS and by expert A and four more experts with less experience than expert A (called B,C,D,E) independently. The experts denoted the positions of fluorescent cells by mouse clicking at their centers. Thereby six independent lists of cell positions were obtained. To calculate error rates of these detection results one list was selected for the "gold standard". We used three different gold standards to evaluate both the NCDS's and the expert's performance:

- a) The detection result of expert A was selected as the gold standard because of his outstanding experience in interpreting fluorescence images.
- b) The detection result of expert B who has a medium image evaluation experience was selected as the gold standard.
- c) By merging the five lists of all experts into a new list we simulated a sixth expert ("OR-expert"). Only those cell positions were written to this list which were included in more than one expert list so that at least two experts had consensus about this fluorescent cell. Identical cells in different expert lists were found by a local nearest neighbor search in the positions. If the Euclidean distance of the two cells at  $p_i$  and  $p_j$  was less than 5 pixels the two positions were merged to one position at  $(p_i + p_j)/2$  in the OR-expert list.

Following [35], two measures were calculated to characterize detection performance based on our gold standard for the human experts and for our system.

**SS:** The sensitivity (SS) of a detector is the percentage of cells of the gold standard which were found by the detector.

**PPV:** The positive predictive value (PPV) is the percentage of detected cells which were also included in the gold standard.

Both SS and PPV were calculated for each human detection and for the NCDS's detection using the gold standards a) and b).

#### IV. RESULTS

We have analyzed human cryostat tissue sections from inflammatory skeletal muscle tissue and from the tonsil for presence of lymphocytes fluorescently labeled for cell surface antigens. Immunofluorescence features of the lymphocytes were inherently different in these tissue types. In the inflamed skeletal muscle arrays of lymphocytes were accumulating within the connective tissue surrounding individual muscle fibers (figure 6a). The latter remained free of any fluorescence label, whilst the fluorescence signals were restricted to the lymphocytes surfaces, indicating specificity of the labeling procedure ([12],[13]). By contrast in a cross-sectioned T-cell area of the tonsil, densely clustering lymphocytes were seen (figure 6b). Muscle tissue- and tonsil tissue-sections, both labeled for CD4 cell surface antigens, were subjected to our learning algorithm at low and high magnifications, respectively. The magnification for muscle sections was 97 $\times$  (figure 6a), and 242 $\times$  for the tonsil (figure 6b) in order to examine the influence of cell magnification

to appear in IEEE Trans. on Information Technology in Biomedicine

TABLE I

ANALYSIS OF THE DETECTION RESULTS OF THE FOUR HUMAN EXPERTS (B-E) AND THE NCDS BY COMPARISON TO THE RESULT OF EXPERT A.

	B	C	D	E	NCDS
SS	0.73	0.70	0.78	0.20	0.97
PPV	0.45	0.58	0.60	0.93	0.26

on the validity of the NCDS.

The results of the cross validation are shown in figure 5 (muscle, figure 5a; tonsil, figure 5b).

The histograms indicate that 90–95% of the positive training samples of  $\Gamma_{test}$  ( $test = 1 \dots 6$ ) are classified correctly for both tissue types. The rates of the correctly rejected negative samples were 80–87%. As indicated in figure 5 there is considerably low intra- and inter-individual variation of classification rates. To compare the expert's and the NCDS's detection performances, the NCDS was trained with a given data set obtained by manual selection of cells carried out by expert A. The NCDS-detected positions of fluorescent cells were denoted by white boxes in the

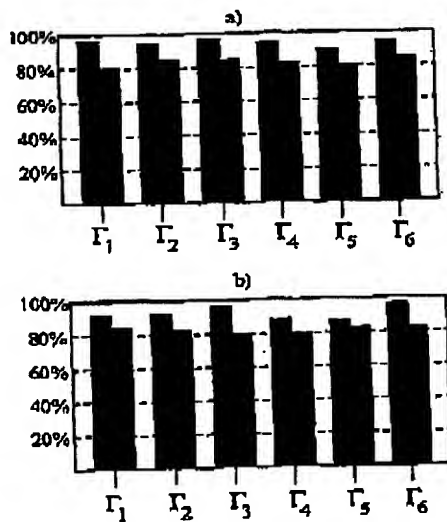


Fig. 5. The histograms representing the classification rates of the NCDS of the six test sets  $\Gamma_i$  for the muscle invading (a) and clustering lymphocytes in the tonsil (b). The black boxes are the classification rates for the positive test samples (true positives) while the grey ones stand for the rate of the negative samples (true negatives) for each test set  $\Gamma_i$ .

TABLE II

ANALYSIS OF THE DETECTION RESULTS OF THE FOUR HUMAN EXPERTS (A,C-E) AND THE NCDS BY COMPARISON TO THE RESULT OF EXPERT B.

	A	C	D	E	NCDS
SS	0.51	0.51	0.51	0.13	0.96
PPV	0.74	0.68	0.63	0.92	0.32

TABLE III

ANALYSIS OF THE DETECTION RESULTS OF THE FIVE HUMAN EXPERTS (A-E) AND NCDS IN COMPARISON TO A SIMULATED OR-EXPERT.

	A	B	C	D	E	NCDS
SS	0.70	0.80	0.78	0.80	0.16	1.00
PPV	0.92	0.65	0.84	0.80	0.96	0.26

images (see figure 6a and 6f). The positions of the detected cells were carefully inspected by expert A and to his evaluation result the PPV of the NCDS was estimated to be greater than 90% and the SS to be 95%.

The results of the comparison of experts and NCDS to gold standards a), b) and c) are shown in Table I, II and III. Although the detection results of experts A and B show considerable variation (see first column of I and II) the classifier trained with expert A's data shows very good generalization performance in reaching similar SS and PPV values for gold standards a) and b). In a next step we aimed at the evaluation of inter-individual detection reproducibility of visual cell detection on a screen showing intensity images. Also it is shown in Table I and II there is a considerable variation in the detection results between all individual experts indicating low reproducibility (for more details see table captions and the Discussion V). For a more objective study we constructed a new gold standard ("OR-expert") containing all cells detected by at least two experts (cf. section III-F). The resulting table III indicates that again, there is substantial inter-individual variation of cellular detection. Approximately only 20% of all cells were reproducibly recognized by all experts. To complete the series of experiments we have used the algorithm for CD4 signal recognition to detect cells immunofluorescently labeled for CD3 (see figure 7a). As shown in figure 7b it is readily seen that the number of correctly recognized cells is above 90% as substantiated by direct evaluation of expert A.

For a 658 × 517-sized image with patch size  $N = 15$

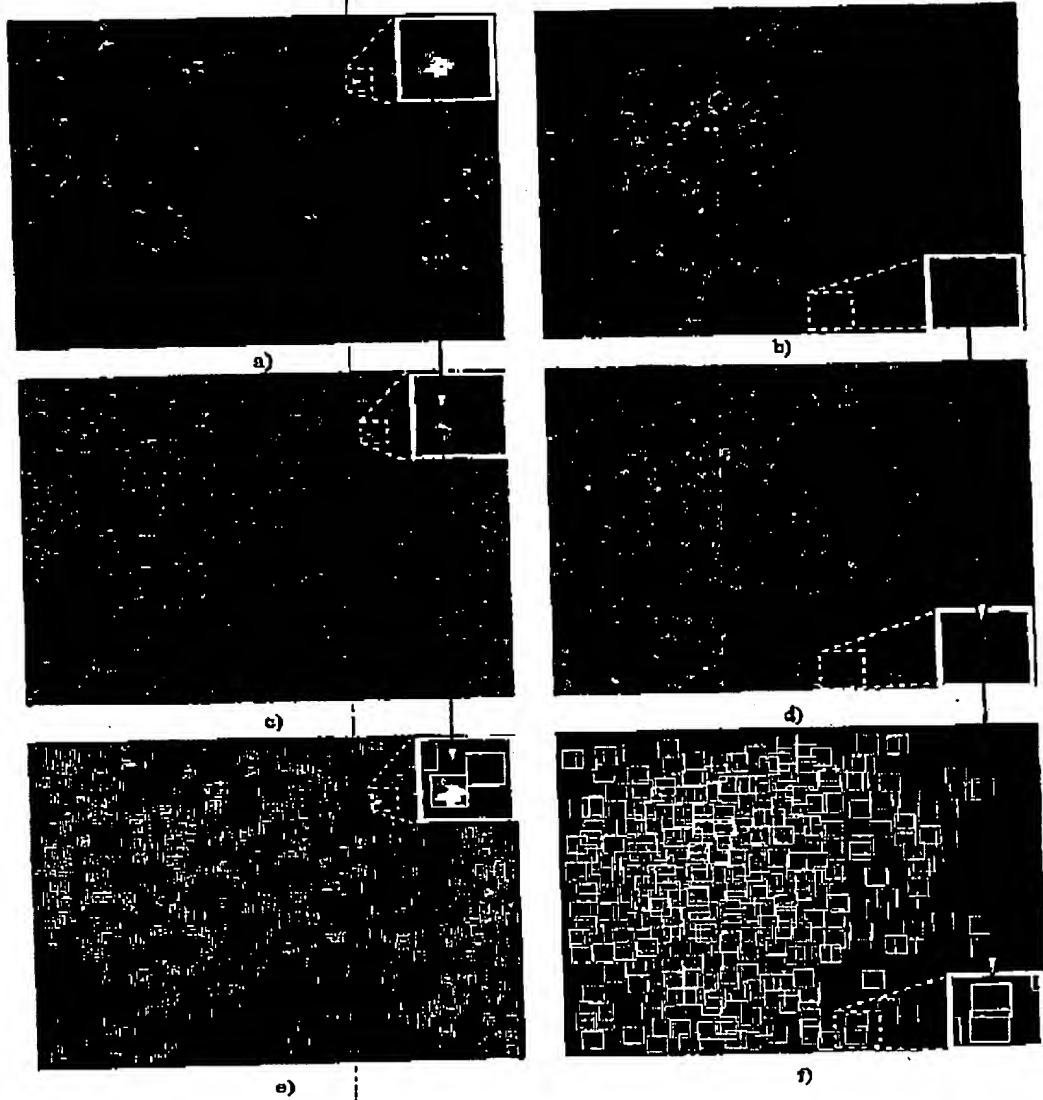
to appear in *IEEE Trans. on Information Technology in Biomedicine*

Fig. 6. Three steps of cell detection for lymphocytes in muscle tissue and tonsil tissue are illustrated: The first row shows the two input images recorded by our standardized technique of (a) muscle invasive lymphocytes and (b) tonsil tissue forming dense clusters within the tonsil. In both experiments the cells were immunolabeled against CD4. In the second row the evidence maps for the muscle invasive cells (c) and the clustering cells in the tonsil (d) are presented. The evidence values  $G(x) \in [0; 1]$ , calculated by our neural classifier were mapped to grey values. A high value stands for a high evidence for a fluorescent cell. The large white boxes in the corners show enlarged regions of each image and evidence map respectively. Following the arrows one can observe that high evidences correspond to positions of fluorescent cells. Local maximum analysis and thresholding delivers the final cell positions within white frames, for both muscle tissue (e) and tonsil (f).

BEST AVAILABLE COPY

to appear in IEEE Trans. on Information Technology in Biomedicine

as a rough estimate of cells maximum diameter the training of the LLM takes one minute, the processing of an image takes two minutes on a standard PC equipped with an AMD K6/300 processor with 96MB RAM. The number of nodes of the LLM was set to  $n = 25$  because the LLM showed best classification performance in this case.

#### V. DISCUSSION

In the present paper we have described a fast and easy to handle algorithm for rapid detection of fluorescent lymphocytes in tissue sections. The detection time of a visual field is approximately two minutes enabling the evaluation of at least 40.000 cells within three hours. The performance speed of the NCDS grows quadratically with the neighborhood size  $N$ , so that an image is analyzed in  $O(N^2)$  steps. The most time-consuming operation is the calculation of the feature vectors. Because this is done by scalar multiplication, a speed-up can be obtained by specialized hardware. The evaluation of one image includes simultaneously (i) the number of cells, (ii) the molecular phenotype of these cells, and (iii) the precise positions of these cells in the x,y-direction in given tissue sections. This direct topological high-throughput-approach enables us to investigate hidden relationships between structure, molecular expression and function. For example, in polymyositis, a human inflammatory disease, it has been shown that invasive T-lymphocytes migrating in the leading front of an army of invasive T-lymphocytes express a cell surface phenotype, which is specific for these front T-cells [13]. T-cells behind this invasive front express substantially different receptor proteins at their cell surface. This indicates clearly that there is a strict dependency between the relative positions of pathogenic T-cells and the phenotypes expressed by them [13]. Similar interrelationships are observed in secondary immune organs such as the tonsil, where T-lymphocytes and B-lymphocytes expressing different protein receptors (CD-antigens) at the cell surface are differentially ordered into specified tissue areas, referred to as the T-cell- and the B-cell-areas [36]. These two examples show that dependencies between structure, molecular expression and function can be visualized by fluorescence microscopy. However, it must be considered, that at present we are not aware of most of the relationships between tissue environment, multicellular molecular phenotype and topology. This is clearly the case in inflammatory infiltrates which are diffusely distributed in the tissue such as in our present ex-

ample of sarcoid myopathy. A systematic analysis would require highly standardized visualization protocols and topological analysis of high reproducibility to generate valid multi-dimensional data-spaces. In our present paper we provide an appropriate system for the latter processes for enabling efficient data-mining and visualization.

Several lines of evidence indicate that the NCDS algorithm works with high precision in individually structured tissues and builds an essential part for extraction of reproducible data from fluorescence micrographs. First, the results of the cross validation show that the neural net performs a satisfactory generalization on the data. The system's classification rates remain constant under variation of training-data. This is an important feature of the NCDS, because in practice the training sets collected for adaptation are generated from different users, so that the sets show variation. The small variations between the classification rates show that the NCDS's detection performance remains constant against these variations. The small variation between rates calculated for training sets of the lymphocytes invading muscle tissue and clustering within the tonsil show that the NCDS also delivers data of constant accuracy under variation of scales considered here.

The lower classification rates on negative samples in both image ensembles show that the LLM's classification is more sensitive than the experts.

Second, we demonstrate that image evaluation by experts show high variation indicating low reproducibility. Therefore automation of the detection process is necessary for valid statistical analysis. The detection performances of experts A-E are discussed briefly in the following. Looking at table I, it is surprising that the values for SS and/or PPV with A being selected for gold standard are rather low. The results can be divided into three groups. Experts B, C and D show similar SS-PPV proportions although with high variances. Expert E achieves the best rate in detecting cells of the gold standard (93%), but at the expense of a very "conservative" decision behavior he misses 80% of the gold standard cells. The third group is the NCDS which has the best SS-rate but seems to pay the price for this by having a low PPV. Table III shows a similar pattern of detection performances. It is interesting to observe that the PPV rates increase while the SS-rates mainly remain constant for all human detectors in relation to table I. This indicates that many cells that were detected by more than one expert were missed by others. This clearly shows

---

*to appear in IEEE Trans. on Information Technology in Biomedicine*

---

that none of the human detectors is valid for a gold standard. Even a simulated OR-expert provides no further improvement, because it leads to the setting of new parameters like the nearest neighbor-distance. The reason for these unreproducible results obtained by the experts is that visual evaluation of grey value images is very tiresome leading to significant decrease of visual attention even within ten minutes of work. Third, visual inspection of the NCDS's detection results led us to much better performance values of SS and PPV for the system than for any of the experts. The difference to the SS- and PPV-values which were based on comparison with both gold standards is not surprising here, because it underlines the inaccuracy of human evaluation used for the gold standard.

The highly inaccurate results obtained by human experts in relation to the demonstrated reproducibility of our system shows that the NCDS can pave the way towards a more systematic analysis of cellular systems in their correct tissue specific environment.

Since the results of the NCDS show high accuracy and reproducibility the system is established in routine work in our lab and its efficiency is controlled in a closed loop between development and application. Because our work aims at the development and improvement of an evaluation tool for a particular image domain, fluorescence micrographs of tissue sections, it is very difficult to compare the algorithm with approaches in related domains as mentioned in chapter I. Because the fluorescence images contain very much noise and the shapes and sizes of the lymphocytes show very much variation the algorithms are definitely not applicable or must be tuned to such a great extent that a comparison would be out of the scope of this article.

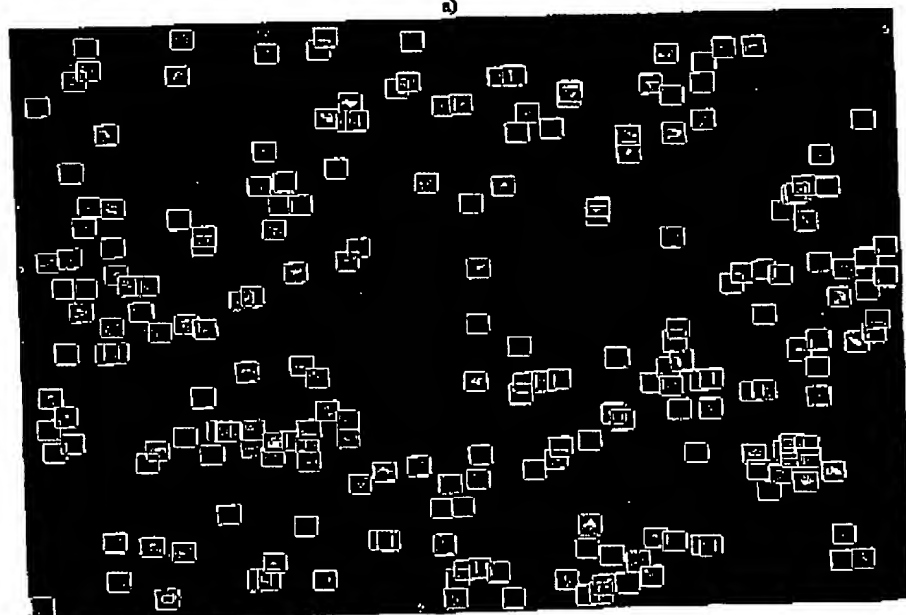
Given the cellular immune system the lymphocytes are organized in different compartments including secondary immune organs and the blood. Hitherto, large-scale cellular phenotype analysis has been restricted to flow cytometry automatic quantitation of lymphocytes in the blood or other types of liquids. We now provide a tool to extend automatic quantitative lymphocyte analysis to the tissue compartments of the immune system.

#### VI. ACKNOWLEDGMENTS

This work was supported by the DFG grants GK-231, Schu627/8-2, BMBF 07NBL04, BMBF 0311951, SFB 387 (TPB1).

to appear in *IEEE Trans. on Information Technology in Biomedicine*

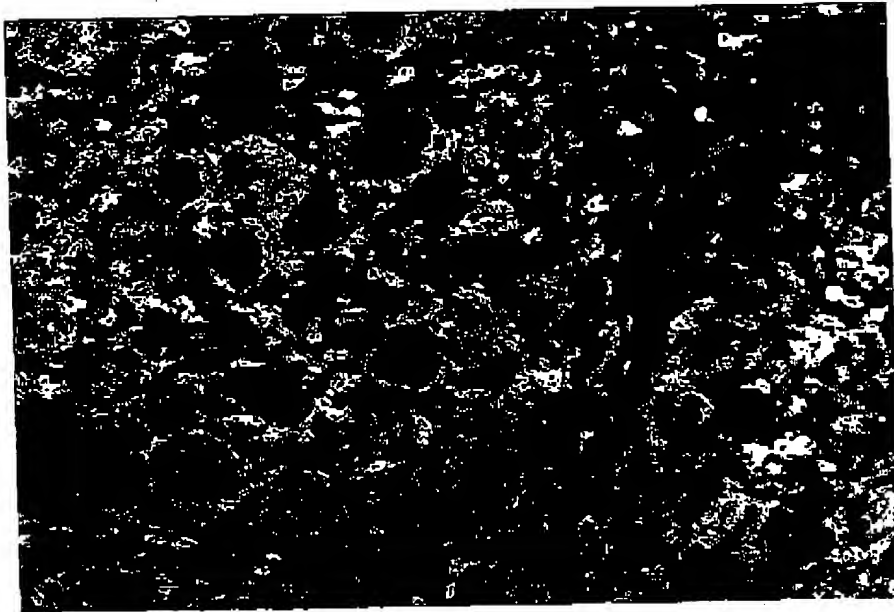
APPENDIX



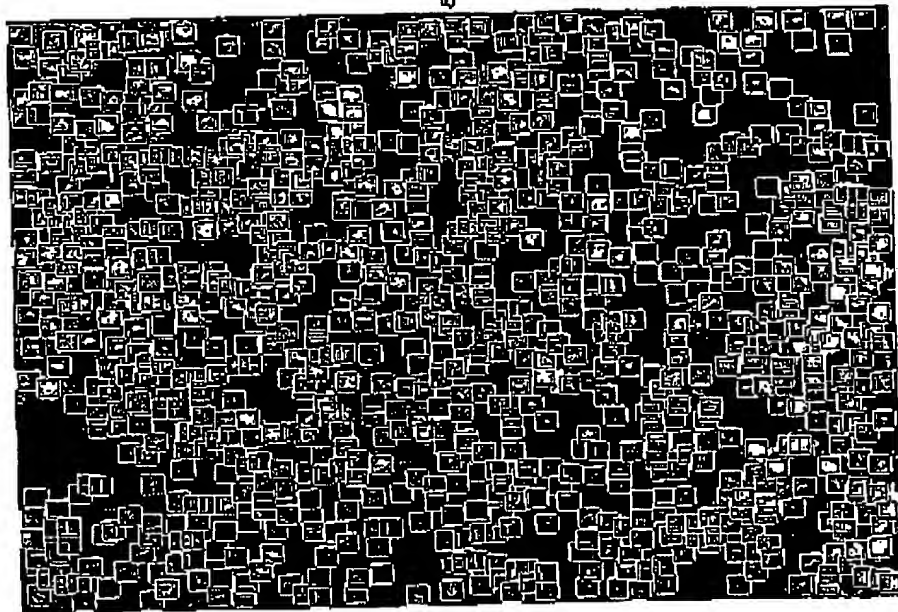
b)

Fig. 7. Above: Muscle-invasive T-lymphocytes immunolabeled for CD3. Below: The cells, detected by the NCDS are surrounded by white boxes. The images have enhanced contrast for better exhibit.

BEST AVAILABLE COPY

**BEST AVAILABLE COPY**to appear in IEEE Trans. on Information Technology in Biomedicine

a)



b)

Fig. 8. Above: Muscle-invasive T-lymphocytes immunolabeled for CD4. Below: The cells, detected by the NCDS are surrounded by white boxes. The images have enhanced contrast for better exhibit.

to appear in *IEEE Trans. on Information Technology in Biomedicine*

## REFERENCES

[1] A. Orfao, G. Schmitz, B. Brando, A. Ruiz-Arguelles, G. Basso, R. Braylan, G. Rothe, F. Lacombe, F. Lanza, S. Papa, F. Lucia, and J.F. San Miguel, "Clinically useful information provided by the flow cytometric immunophenotyping of hematological malignancies: current status and future directions," *Clin. Chem.*, vol. 45, no. 10, pp. 1708-1717, Oct. 1999.

[2] J.A. Viedma Contreras, "Leucocyte activation markers in clinical practice," *Clin. Chem. Lab. Med.*, vol. 37, no. 6, pp. 607-622, Jun. 1999.

[3] D. Campiani and E. Coustan-Smith, "Detection of minimal residual disease in acute leukemia by flow cytometry," *Cytometry*, vol. 38, no. 4, pp. 139-152, Aug. 1999.

[4] M.J. Jarneski and G. Radcliff, "Fundamentals of flow cytometry," *Mol. Biotechnol.*, vol. 11, no. 1, pp. 37-57, Feb. 1999.

[5] N. Zurgil, Y. Levy, M. Deutsch, B. Gilburt, J. George, D. Harats, M. Kaufman, and Y. Shoenfeld, "Reactivity of peripheral blood lymphocytes to oxidized low-density lipoprotein: a novel system to estimate atherosclerosis employing the cellscan," *Clin. Cardiol.*, vol. 22, no. 8, pp. 526-532, Aug. 1999.

[6] K.V. Mardia, Wei Qian, D. Shah, and K.M.A. da Souza, "An algorithm for dividing clusters fluorescent stained nuclei," *IEEE Transactions on Pattern Analysis and Machine Intelligence*, vol. 19, pp. 1035-1042, 1997.

[7] A.I. Dow, S.A. Shafer, J.M. Kirkwood, Mascari R.A., and A.S. Waggoner, "Automatic multiparameter fluorescence imaging for determining lymphocyte phenotype and activation status in melanoma tissue sections," *Cytometry*, vol. 25, pp. 71-81, 1996.

[8] K. Hanashara and M. Hiyama, "A circle-detection algorithm simulating wave propagation," *Machine Vision and Applications*, vol. 3, pp. 97-111, 1990.

[9] W. Galbraith, M.C.E. Wagner, J. Chao, M. Abaza, L.A. Ernst, M.A. Nederlof, R.J. Hartsock, D.L. Taylor, and A.S. Waggoner, "Imaging cytometry by multiparameter fluorescence," *Cytometry*, vol. 12, pp. 579-596, 1991.

[10] G. Gerig and F. Klein, "Fast contour identification through efficient Hough transform and simplified interpretation strategy," *Proc. Int. Conf. on Pattern Recognition*, vol. 8, pp. 498-500, 1986.

[11] D. H. Ballard, "Generalizing the Hough transform to detect arbitrary shapes," *Pattern Recognition*, vol. 13, pp. 111-121, 1981.

[12] W. Schubert, K. Zimmermann, M. Cramer, and A. Starzinski-Powitz, "Lymphocyte antigen leul9 as a molecular marker of regeneration in human skeletal muscle," *Proc. Natl. Acad. Sci. USA*, pp. 307-311, 1989.

[13] W. Schubert, C. L. Masters, and K. Bayreuther, "App+ t-lymphocytes selectively sorted endoneurial tubes in polymyelitis displace acm expressing muscle fibres," *Eur. J. Cell Biol.*, vol. 58, pp. 395-410, 1993.

[14] D. Dunn, W. E. Higgins, and J. Wakely, "Texture segmentation using 2d Gabor elementary functions," *IEEE Transactions on Pattern Analysis and Machine Intelligence*, vol. 16(2), pp. 130-149, Feb. 1994.

[15] Tal Sing Lee, "Image representation using 2d Gabor wavelets," *IEEE Transactions on Pattern Analysis and Machine Intelligence*, vol. 18(10), pp. 959-971, Oct. 1996.

[16] R. Rao and D. Ballard, "An active vision architecture based on iconic representations," Tech. Rep., University of Rochester CS, 1995.

[17] M. Turk and A. Pentland, "Eigenfaces for recognition," *Journal of Cognitive Neuroscience*, vol. 3, pp. 71-86, 1991.

[18] H. Varchmin, Axel C., Robert Rae, and Helge Ritter, "Facial feature detection using neural networks," in *Proc. Intern. Conf. on Art. Neur. Netw. Lausanne*, Martin Hasler, Wulfrao Geistner, Alain Germond and Jean-Daniel Nicoud, Eds. 1997, pp. 955-960, Springer.

[19] Helge Ritter, "Learning with the self-organizing map," in *Artificial Neural Networks 1*, T. Kohonen, Ed. 1991, Elsevier Science Publishers, B.V.

[20] G. Heidemann and H. Ritter, "Combining multiple neural nets for visual feature selection and classification," in *ICANN 99, Ninth International Conference on Artificial Neural Networks*, 1999, pp. 365-370.

[21] T. Kohonen, *Self-Organization and Associative Memory*, Springer-Verlag, Berlin, 1989.

[22] T. Kohonen, "Self-organized formation of topologically correct feature maps," *Biol. Cybernetics*, vol. 43, pp. 59-69, 1982.

[23] C. M. Bishop, "Gtm: the generative topographic mapping," *Neural Computation*, vol. 10, no. 10, pp. 215-234, 1998.

[24] P. Demartines and J. Herault, "Curvilinear component analysis: A self-organizing neural network for nonlinear mapping of data sets," *IEEE Trans. on Neural Networks*, vol. 8, no. 1, pp. 148-154, 1997.

[25] N. R. Pal and V. K. Bhuri, "Two efficient connectionist schemes for structure-preserving dimension reduction," *IEEE Trans. on Neural Networks*, pp. 1142-1154, 1997.

[26] J. W. Sammon Jr., "A non-linear mapping for data structure analysis," *IEEE Transactions on Computers*, C-18, pp. 401-409, 1969.

[27] J. Mao and K. Jain, "Artificial neural networks for feature extraction and multivariate data projection," *IEEE Trans. on Neural Networks*, vol. 6, no. 2, pp. 200-217, 1995.

[28] E. Oja and S. Kaski, *Kohonen Maps*, Elsevier Publisher, 1999.

[29] D.E. Rumelhart, G.R. Hinton, and R.J. Williams, "Learning internal representations by error propagation," *Parallel Distributed Processing: Explorations in the Microstructure of Cognition*, vol. 1: Foundations, pp. 318-362, 1986.

[30] J.B. Moody and C.J. Darken, "Fast learning in networks of locally-tuned processing units," *Neural Computation*, vol. 1, no. 2, pp. 281-294, 1989.

[31] Günther Heidemann, *Ein flexibel einsetzbares Objekterkennungssystem auf der Basis neuronaler Netze* (in german), Ph.D. thesis, Universität Bielefeld, Technische Fakultät, 1988, Infor, DISKI 190.

[32] G. Heidemann and H.J. Ritter, "Efficient vector quantization using the wha-rule with activity equalization," *Neural Processing Letters*, 2000, To appear.

[33] M. Stone, "Cross-validation choice and assessment of statistical predictors," *Journal of the Royal Statistical Society*, vol. 36, pp. 111-147, 1974.

[34] H. M. Zweig and G. Campbell, "Receiver-operating characteristic (roc) plots: A fundamental evaluation tool in clinical medicine," *Clin. Chem.*, vol. 39, no. 4, pp. 561-577, 1993.

[35] F. Schmorrenberg, C.S. Pattichis, K. Kyriakou, and C.N. Schizas, "Computer-aided detection of breast cancer

to appear in IEEE Trans. on Information Technology in Biomedicine

clei," *IEEE Trans. on Inf. Techn. in Biomedicine*, vol. 1,  
no. 2, pp. 128-140, 1991.  
[36] M. Petty and A. Whyte, "Immunology of the tonsils,"  
*Immunol. Today*, vol. 19, pp. 414-426, 1989.

# Automatic Recognition of Muscle-invasive T-lymphocytes Expressing Dipeptidyl-peptidase IV (CD26) and Analysis of the Associated Cell Surface Phenotypes

W. SCHUBERT<sup>a,b,\*</sup>, M. FRIEDENBERGER<sup>a</sup>, R. HAARS<sup>a</sup>, M. BODE<sup>b</sup>, L. PHILIPSEN<sup>b</sup>, T. NATTKEMPER<sup>c</sup> and H. RITTER<sup>c</sup>

<sup>a</sup>Institute of Medical Neurobiology, Molecular pattern recognition research group, Otto-von-Guericke University of Magdeburg, ZENT-Building, Leipziger Str. 44, 39120 Magdeburg, Germany; <sup>b</sup>MECTAC Ltd, ZENT-Building, Leipziger Str. 44, 39120 Magdeburg, Germany; <sup>c</sup>Neuroinformatics group, University of Bielefeld, 33519 Bielefeld, Germany

(Received 1 August 2000; in final form 29 April 2001)

A neural cell detection system (NCDS) for the automatic quantification of fluorescent lymphocytes in tissue sections was used to analyze CD26 expression in muscle-invasive T-cells. CD26 is a cell surface dipeptidyl-peptidase IV (DPP IV) involved in co-stimulatory activation of T-cells and also in adhesive events. The NCDS system acquires visual knowledge from a set of training cell image patches selected by a user. The trained system evaluates an image in 2 min calculating (i) the number, (ii) the positions and (iii) the phenotypes of the fluorescent cells. In the present study we have used the NCDS to identify DPP IV (CD26) expressing invasive lymphocytes in sarcoid myopathy and to analyze the associated cell surface phenotypes. We find highly unusual phenotypes characterized by differential combination of seven cell surface receptors usually involved in co-stimulatory events in T-lymphocytes. The data support a differential adhesive rather than a co-stimulatory role of CD26 in muscle-invasive cells. The adaptability of the NCDS algorithm to diverse types of cells should enable us to approach any invasion process, including invasion of malignant cells.

**Keywords:** Muscle; CD26; Neural network; Image analysis; Inflammatory myopathy

## 1. INTRODUCTION

Dipeptidyl-peptidase IV (DPP IV, CD26) is a cell surface transmembrane protein characterized by a short N-terminal cytoplasmic domain and a long extra cellular region with a sugar rich and a Cys-rich domain. A third 260 aminoacid C-terminal extra cellular region was found to exhibit DPP IV enzymic catalytic activity. (Hegen *et al.*, 1990; Darmoul *et al.*, 1992; Tanaka *et al.*, 1992). DPP IV is a member of the prolyl oligopeptidase family which is defined by the requirement of the catalytic triad in the unique order Ser, Asp, His (Abbott *et al.*, 1994). The enzyme cleaves amino-terminal dipeptides with either L-proline or L-alanine in the penultimate position.

DPP IV has been shown to be expressed by a variety of cell types including T- and B-lymphocytes, activated NK cells, and by epithelia of the intestine, the prostate, and the

proximal tubuli of kidneys (Stein *et al.*, 1989; Hegen *et al.*, 1990; Bühling *et al.*, 1995). DPP IV is implicated in inflammatory processes and appears to play a part in the progression of certain malignant tumors (Morrison *et al.*, 1993; Iwata and Morimoto, 1999). Given the cellular immune response (Morimoto and Schlossman, 1998), an important function of DPP IV is its role as a co-stimulatory cell surface protein that is involved in the activation of the T-lymphocyte.

Within the T-cell activation cascade, antibody-induced stimulation of DPP IV leads to tyrosine phosphorylation of several intracellular proteins with a similar pattern to that seen after stimulation of the T-cell antigen receptor (TCR)/CD3 complex of CD4- or CD8-expressing T-cells (Hegen *et al.*, 1997). Given stimulation of T-cells via this complex, CD26 provides a true co-stimulatory function that can up-regulate the signal-transducing properties of the TCR.

\*Corresponding author. Address: Institute of Medical Neurobiology, Molecular pattern recognition research group, Otto-von-Guericke University of Magdeburg, ZENT-Building, Leipziger Str. 44, 39120 Magdeburg, Germany. Tel.: +49-391-6117-174. Fax: +49-391-6117-176. E-mail: wschubert@pc.mdu.mpg.de

TABLE I CD cell surface antigen analyzed in this study

CD antigen	Specificity	Monoclonal antibody clone
CD 26	DPP IV: adhesive diaminopeptidase binding protein	L272
CD 8	Co-recognition receptor for MHC class I with TCR	B9.11
CD 4	Co-recognition receptor for MHC class II with TCR	13B8.2
CD 11 b	$\alpha$ M integrin chain of MAC-1 complex, C3bi receptor "CR3"	44
CD 19	Receptor of the Slg family, modulates B cell responsiveness	J4.119
CD 2	SRBC receptor, ligand for LFA 3 (CD58)	39C1.5
CD 3	Signal transduction receptor complex associated with TCR	UCHT1

In peripheral blood the T-lymphocytes that express DPP IV are either CD4 or CD8 positive cells, and, as a rule show co-expression of intact TCR/CD3 complexes. Hence a T-cell that can be co-stimulated via CD26 is a CD4<sup>+</sup>/CD3<sup>+</sup>/TCR<sup>+</sup>/CD26<sup>+</sup> or a CD8<sup>+</sup>/CD3<sup>+</sup>/TCR<sup>+</sup>/CD26<sup>+</sup> T-cell. In addition, the majority of these T-cells also express CD2, which can provide an alternative pathway of T-cell activation (Davis *et al.*, 1998).

In the present paper we have addressed the expression of DPP IV and DPP IV-associated cell surface phenotypes in muscle-invasive T-lymphocytes. Multi-epitope imaging microscopy (Schubert, 1992) was used to co-localize seven different cell surface proteins including CD26 on the cell surface of these muscle-invasive T-cells. The latter technology was coupled to a new learning algorithm (Nattkemper *et al.*, 1999, 2000a), which automatically recognizes T-cells within tissue sections obtained from patients suffering from chronic inflammatory muscle disease. We have selected chronic sarcoid myopathy, which represents a human disease type showing T-lymphocyte invasion of the muscle tissue. The T-lymphocytes are present to a large extent within the connective tissue between the muscle fiber fascicles, a space that is defined as the perimysium. In addition, sarcoid myopathy is characterized by the formation of giant cells, that is supposed to be driven by the cooperation between T-cells and macrophages (Wahlstrom *et al.*, 1999).

In the present study we have examined whether muscle-invasive T-lymphocytes exhibit a cell surface phenotype required for T-cell activation and CD26-associated T-cell stimulation. Using a library of seven different monoclonal antibodies we find that the majority of the T-cells do not co-express the cell surface receptor sets, which would be required for T-cell activation via the co-stimulator molecule CD26. Instead these T-cells express unusual cell surface phenotypes by heterogeneous receptor combinations, most of which are minus-variants of the phenotypes found in the blood. We suggest that these "unusual" cell surface phenotypes are involved in differential adhesion mechanisms and T-cell migration rather than T-cell activation.

We also describe a learning algorithm, by which T-cells within the tissue can be automatically recognized and quantified. Given that a large number of tissue sections

have to be mapped by multi-epitope imaging, the algorithm opens the possibility for high-throughput screening of invasive lymphocytes in tissues (Nattkemper *et al.*, 2000a). The adaptability of the algorithm to diverse types of cells should enable us to approach any invasion process, including invasion of malignant cells.

## 2. IMAGING METHODS

In order to address the CD26-associated phenotype of muscle-invasive T-cells, we have applied seven monoclonal antibodies directed against cell surface antigens (CD antigens) in cryosections of diagnostic biopsies. The antigens are listed in Table I. All antibodies were directly conjugated to dyes and applied to the tissue sections as described earlier (Schubert, 1992). Each fluorescent signal was recorded as a digitized image by a cooled CCD camera. Fluorescent cells were either localized by medical experts using a mouse-delineation of the fluorescent area, or were automatically recognized by the learning algorithm described below.

## 3. AUTOMATIC T-CELL FLUORESCENCE PATTERN RECOGNITION

To identify CD26 positive T-cells and other T-cell types in tissue sections we used a modular computer system that detects the positions of up to 95% of all fluorescent lymphocytes in one given input image  $M$ , the digitized fluorescence micrograph (Nattkemper *et al.*, 1999). The first module of the cell detection system is a trained cell classifier that classifies a square image region  $p$  of  $15 \times 15$  pixels to a so called evidence value  $C(p) \in [0; 1]$  representing the probability that the center of  $p$  is occupied by a fluorescent cell. The second module evaluates the evidence values of all points in  $M$  to a list of positions of fluorescent lymphocytes. The positions of the detected cells are visualized on a screen and stored in a database. In the following subsections we describe the cell detection system briefly, see (Nattkemper *et al.*, 1999, 2000b) for details.

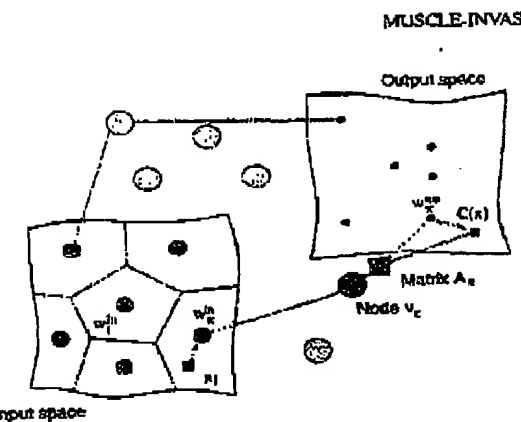


FIGURE 1 Example illustrating a Local Linear Map (LLM) approximating a mapping with six nodes. The LLM's nodes  $v_i^{\text{in}}$  form Voroni cells of the input space. The mapping into the output space is performed by a local linear transformation given by  $A_i$  and  $w_i^{\text{out}}$ . First, the nearest neighbor  $v_i^{\text{in}}$  to the input is selected, then the input is mapped via the coupled matrix  $A_i$ .

#### 4. TRAINING OF THE CELL CLASSIFIER

The cell classifier  $C(p)$  is a trained artificial neural network (ANN). Neural networks have been shown to be powerful classification tools in many industrial computer vision applications. In biomedical image analysis the application of ANNs is not frequent, and only recently applications have been published (Sjøestrom *et al.*, 1999).

To map an image region  $p$  to its evidence value, six numerical feature values are calculated for  $p$  and combined to a so called feature vector  $x \in \mathbb{R}^6$ . Here the term "vector" describes a set of numerical elements as used in the field of computational pattern recognition. The computation of the feature vector is described in 12. The trained ANN computes the evidence value for  $p$  by mapping its feature vector  $x$  to  $C(x)$  using the learned classification mappings  $C : \mathbb{R}^6 \rightarrow \mathbb{R}$ .

The ANN used for cell classification is of Local Linear Map-type (LLM) which was introduced by Ritter (1991) and has been shown to be a powerful tool in fast learning of non-linear mappings.

$$C : \mathbb{R}^{d_{\text{in}}} \rightarrow \mathbb{R}^{d_{\text{out}}},$$

such as classification tasks in Computer Vision applications (Heidemann and Ritter, 1999). The LLM-approach was originally motivated by the Kohonen Self-organizing Map (Kohonen, 1989) with the aim to obtain a good map resolution even with a small number of units. In the LLM learning scheme unsupervised and supervised learning are combined in contrast to the widely used multi-layer perception trained with back-propagation (Rumelhart *et al.*, 1986). The LLM is given through

$$\{w_i^{\text{in}} \in \mathbb{R}^{d_{\text{in}}}, w_i^{\text{out}} \in \mathbb{R}^{d_{\text{out}}}, A_i \in \mathbb{R}^{d_{\text{in}} \times d_{\text{out}}}, i = 1 \dots n\}$$

#### MUSCLE-INVASIVE T-LYMPHOCYTES

69

and a triple

$$v_i = (w_i^{\text{in}}, w_i^{\text{out}}, A_i)$$

is called node. In the present work the LLM parameters are  $d_{\text{in}} = 6$ ,  $d_{\text{out}} = 1$ ,  $n = 25$ .

By calculating

$$C(x) = w_k^{\text{out}} + A_k(x - w_k^{\text{in}})$$

the input feature vector  $x$  is mapped to the evidence value  $C(x)$ , & holds

$$k = \arg \min \{ \|x - w_i^{\text{in}}\| \},$$

so  $w_k^{\text{in}}$  is the nearest neighbor to input  $x$ . An illustration is given in Fig. 1.

The three free parameters of each of the  $n$  nodes

$$(w_i^{\text{in}}, w_i^{\text{out}}, A_i, i = 1 \dots n)$$

are trained with a pre-selected set  $\Gamma$  of  $m$  (input, output)-pairs.

$$\Gamma = \{(x_\alpha, y_\alpha)\}, \alpha = 1 \dots m$$

that is composed of two subsets  $\Gamma = \Gamma^{\text{pos}} \cup \Gamma^{\text{neg}}$ . The so called positive set

$$\Gamma^{\text{pos}} = \{(x_\alpha^{\text{pos}}, 1)\}$$

consists of feature vectors  $x_\alpha^{\text{pos}}$  computed (see below) from image patches centered at positive training samples for fluorescent cells, together with the target output value

$$y_\alpha^{\text{pos}} = C(x_\alpha^{\text{pos}}) = 1$$

of the classifier. The negative set

$$\Gamma^{\text{neg}} = \{(x_\alpha^{\text{neg}}, 0)\}$$

consists of feature vectors  $x_\alpha^{\text{neg}}$  computed from non-cell image patches (see below) and their target classification output value

$$y_\alpha^{\text{neg}} = C(x_\alpha^{\text{neg}}) = 0.$$

To obtain  $13 \times 15$  sized image patches for computing, the feature vectors  $x_\alpha^{\text{pos}} \in \Gamma^{\text{pos}}$  are an interactive program displaying the digitized microscope fluorescence images and allowing users to select cell centers with the aid of a mouse cursor. The set  $\Gamma^{\text{pos}}$  is then generated automatically by randomly selecting image points in a minimum distance of  $r_{\text{neg}} = 5$  pixels from any of the selected cells of  $\Gamma^{\text{pos}}$ . For each of these randomly selected points a feature vector  $x_\alpha^{\text{neg}}$  is computed by the same procedure as for  $\Gamma^{\text{pos}}$ . In one training step of the LLM first one input-output pair  $(x_\alpha, y_\alpha)$  is selected randomly from the training set  $\Gamma = \{(x_\alpha, y_\alpha)\}$ , secondly the best-match node  $v_k$  is found, and third its weights are changed according to the

BEST AVAILABLE COPY

70

W. SCHUBERT et al.



FIGURE 2 12 lymphocytes calculated from manual mouse-click selection of 120 cross-sectioned lymphocytes.

following learning rules

$$\Delta w_k^{in} = \epsilon^{in} (x_\alpha - w_k^{in}) \quad (1)$$

$$\Delta w_k^{out} = \epsilon^{out} (y_\alpha - C(x_\alpha)) + A_k \Delta w_k^{in} \quad (2)$$

$$\Delta A_k = \epsilon^A (y_\alpha - C(x_\alpha)) \frac{(x_\alpha - w_k^{in})^T}{\|x_\alpha - w_k^{in}\|^2} \quad (3)$$

with  $\epsilon^{in}, \epsilon^{out}, \epsilon^A \in [0, 1]$  as exponentially decreasing learning step sizes. Looking at the rules, one can observe that learning rule (1) is an online version of k-means (Moody and Darken, 1989) for positioning the  $n$  centers of  $w_k^{in}$ . And (2) and (3) adjust a linear mapping specified by vector  $w_k^{out}$  and matrix  $A_k$  in the vicinity (Voronoi cell) around the best match node.

## 5. CALCULATION OF CELL FEATURES

In the development of a classification system a suitable feature computation is crucial for the performance of the system. In the context of this work the cell features should be robust against small changes of size, intensity and curvature of the fluorescent cells in the  $15 \times 15$  patches.

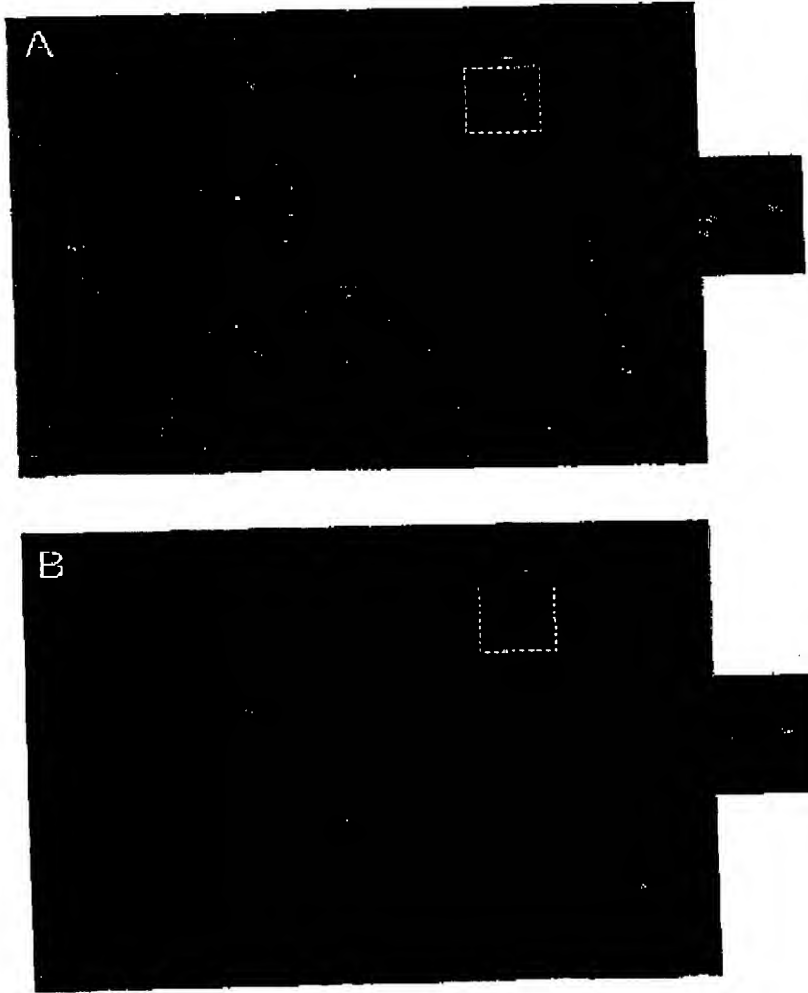


FIGURE 3 (caption opposite)

## BEST AVAILABLE COPY

71

## MUSCLE-INVASIVE T-LYMPHOCYTES

TABLE II Simultaneous detection of 24 T-cell phenotypes expressed different combinations of seven different cell surface receptors

Frequency (%) of T-cell in muscle	Combinatorial phenotype						
	CD2	CD3	CD4	CD8	CD11b	CD19	CD26
35.1	0	0	1	0	0	0	0
29.9	1	0	0	0	0	0	0
13.2	1	0	1	0	0	0	0
5.0	1	1	1	0	0	0	0
3.1	1	0	0	0	1	0	0
2.0	0	0	0	0	0	0	0
1.8	1	0	0	1	0	0	0
1.5	1	1	0	1	0	0	1
1.3	1	1	1	0	0	0	1
1.3	0	0	0	0	0	1	0
1.1	0	0	1	1	0	0	1
0.9	1	0	1	1	0	0	0
0.9	1	0	1	0	0	0	0
0.7	1	1	0	0	0	0	0
0.7	0	1	1	0	1	0	0
0.6	0	0	0	0	0	0	0
0.4	1	1	1	0	0	0	1
0.4	0	0	0	0	1	0	1
0.4	1	0	0	0	0	1	0
0.2	1	0	0	1	0	1	0
0.2	1	0	0	0	1	0	1
0.2	0	0	1	1	0	0	0

Because the cells are in muscle tissue, their size, intensity and shape show considerable variation. One way to map an image point  $p$  to a feature vector  $x \in \mathbb{R}^n$  is to calculate the overlaps of a surrounding image region of size  $15 \times 15$  with a set of 6 filters, such as Gabor filters (Dunn *et al.*, 1994; Lee, 1996) or steerable derivatives of 2-dimensional Gaussians (Rao and Ballard, 1995). The disadvantage of such filters is that they contain several

parameters (radius, orientations, etc.), which have to be fitted according to the particular application. This is difficult and/or time-consuming for a non-expert user. To avoid such problems we use here a Principal Component Analysis (PCA) on a set of  $15 \times 15$ -sized image patches of centered cells, which is a data-driven approach.

In this application the PCA-technique uses 6 eigenvectors  $u_i \in \mathbb{R}^{N^2}$  (so called "eigencells") of the

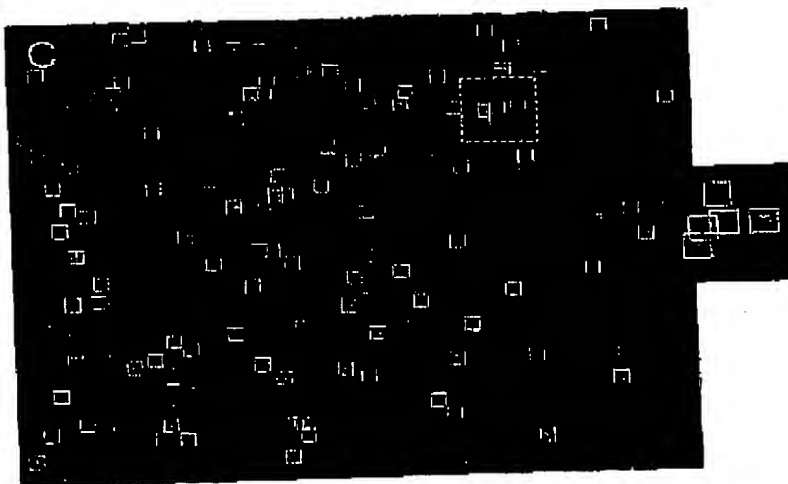


FIGURE 3 The detection of CD26 fluorescent lymphocytes in muscle tissue is illustrated. Figure 3A shows the input image of invading lymphocytes in muscle tissue. The cells were immunolabeled with anti-CD26. The evidence map computed by the LLM is illustrated in Fig. 3B. The evidence values are scaled to [0:255] for visualization purposes. A high value stands for a high evidence of a fluorescent cell. The finally detected positions of fluorescent cells as indicated by white boxes are shown in Fig. 3C. A typical image showing five lymphocytes is shown in the inset on the right hand side of each picture.

covariance matrix of  $15 \times 15$  image patches. The patches are the  $15 \times 15$ -sized image regions around the handselected image points of fluorescent cells which were selected for training (see above). The usage of such eigenvectors is a well-known technique for detection tasks (Turk and Pentland, 1991; Varchmin *et al.*, 1997). A listing of the eigenvalues in descending order reveals that the majority of the variance in the image data is described by the six eigencells of the six highest eigenvalues. Figure 2 shows 6 eigencells computed from the training set. These are taken to generate the 6-dimensional feature vector  $\mathbf{x}$  for an image point by scalar multiplication of its  $15 \times 15$  neighborhood with the six eigencells.

## 6. CELL DETECTION IN FLUORESCENCE MICROGRAPHS WITH THE LLM

For the full automatic detection of CD26 positive cells and other T-cell types in one given micrograph every image point  $p$  is mapped to its evidence value  $[0, 1]$  by calculating the LLM output  $C(x) \in [0, 1]$  for its feature vector  $\mathbf{x}$  of its surrounding  $15 \times 15$ -image patch. Mapping evidences of all points to their corresponding image positions we achieve the so-called evidence map. A point  $p_e$  in the evidence map, which has the highest evidence value  $C(x)$  within a 5-pixel radius above a given evidence threshold  $r_e = 0.5$ , is the result position of the center of one fluorescent cell, so  $C(x)$  obeys

$$C(p) > 0.5 \wedge C(p) = \arg \max\{C(p')\} \quad d(p', p) \leq 5$$

One input micrograph (A), its evidence map (B) and the detected fluorescent cells (C) are shown in Fig. 3.

## 7. RESULTS AND DISCUSSION

In the present paper we have analyzed invasive T-lymphocytes in muscle tissue for the expression of DPP IV (CD26). To analyze the cell surface receptor expression patterns of these T-cells we used the multi-epitope imaging approach (Schubert, 1992), in a new form working at the level of single clearly identifiable cells (details will be published elsewhere). Here we used a limited number of seven monoclonal antibodies to simultaneously detect seven different T-cell surface proteins. By this approach we have addressed the role of CD26 as a co-stimulatory molecule in the T-cell activation cascade. In order to examine, whether muscle-invasive T-cells in sarcoid myopathy do or do not show the expected CD26-associated patterns of receptor expression. This study extends the data obtained by the analysis of lymphocyte associated proteins found to be expressed in muscle tissue (Schubert *et al.*, 1989, 1993; Schubert, 1991; Haars *et al.*, 2000).

The muscle-invasive T-cells were found to be present as low-density infiltrates in the parymyosum of the muscle

tissue. Surprisingly, the majority of these cells were negative for CD26, indicating that activation of T-cells via the CD26 dependent pathway does not play a key role in this disease. CD19<sup>+</sup> B-lymphocytes were rare and these did not express CD26. Together, only 5.4% of the T-cells expressed CD26 (see Table II). These cells showed substantial variation according to differential expression of the six other cell surface receptors (CD2, CD3, CD4, CD8, CD11b). Among the CD26-positive cell fraction, the co-expression of CD3 and CD4 or CD8 and CD3 was seen most frequently, whilst few CD26-positive cells showed co-expression of CD4 or CD8 alone. An unusual T-cell type was seen which shows co-expression of CD2, CD11b and CD26, whilst CD4, CD8 and CD3 were absent in these cells. Finally the vast majority of T-cells, which were negative for CD26 (~95%) also showed a highly unusual phenotype characterized either by expression of CD4 alone, or CD2 alone, whilst co-expression of the CD3 receptor complex was restricted to only a minor fraction of CD4-positive and CD8-positive T-lymphocytes (for summary see Table II).

Together these data show, that muscle-invasive T-lymphocytes in sarcoid myopathy show a highly unusual phenotype at two levels: First, T-lymphocytes in the peripheral blood, that express CD26, are CD4-positive or CD8-positive T-cells which are also characterized by co-expression of the CD3 complex, as a rule, and most of these T-cells also show co-expression of CD2, which is implicated in an alternative pathway of T-cell activation (Davis *et al.*, 1998). In the present study it is shown that within the minor fraction of muscle-invasive T-cells, which show the expression of CD26 (5.6% of all cells), only approximately one half of these cells do show the CD2/CD3/CD4/CD26 or the CD2/CD3/CD8/CD26 phenotype as expected for a fully "equipped" T-cell. The other half of the CD26-positive cells express minus-variants of this pattern, characterized by omission of one or more of the CD3/CD2/CD8 or CD4 receptors. Interestingly, in these cells, CD26 may occur together with the  $\alpha M$  integrin CD11b. It is unclear at present, whether the latter cells are T-cells or macrophages. Together, a fraction of the muscle-invasive T-cells show both cell surfaces that are compatible and others that are not compatible with a role of CD26 as a co-stimulatory signal of T-cell activation.

Second, the majority of T-cells, that have invaded the muscle tissue in sarcoid myopathy are clear-cut minus-variants of the T-cell surface expression patterns normally found in the blood, because these cells *in situ* only express either CD4 or CD2 (together 64% of all invasive T-cells), whilst CD3, CD8, CD11b and CD26 are absent. Another T-cell fraction, which is substantially less frequent is the CD2<sup>+</sup>/CD4<sup>+</sup> (15%) and the CD2<sup>+</sup>/CD3<sup>+</sup>/CD4<sup>-</sup> T-cell type (5%). Only the latter one would reflect the "normal" cell surface expression pattern of a CD4 T-cell. This demonstrates the predominant presence of T-cells, which, as a rule, lack receptor patterns at the cell surface, which would be obligatory for the T-cell activation

## MUSCLE-INVASIVE T-LYMPHOCYTES

73

cascade. Hence, it is very unlikely that T-cells invading the muscle tissue in sarcoid myopathy undergo T-cell activation via the known battery of co-stimulatory receptors.

Alternatively we would like to suggest, that the heterogeneous "unusual" combinatorial receptor phenotypes of the T-cell surface are involved in differential adhesive functions and migratory mechanisms. This view is supported by the fact, that CD26, besides its role as a co-stimulatory signal in T-cell activation, also exerts adhesive functions by binding to collagen (Dang *et al.*, 1990). Adhesive functions have also been assigned to CD2, CD8, CD4 and CD11b (Barclay *et al.*, 1993; Pigott and Power, 1993). We therefore suggest, that all phenotypes detected in muscle tissue in our present study (Table II) are implicated in cell surface "decision-processes" that either fix the T-cell at a certain position in the tissue or promote T-cell migration. The T-cell may acquire this function by differentially combining receptors in a manner illustrated by the data presented in Table II.

The neural classifier used in the present study enables us to analyze CD26<sup>+</sup> and CD26<sup>-</sup> T-cell phenotypes at a large scale. The disease-associated phenotypic data presented here and the NCDS as a high-throughput approach could provide important links for mathematical modeling T-cell invasion at an integrated molecular and cellular level.

## Acknowledgements

We thank F. Wedler for help in preparing the manuscript. The excellent technical assistance of M. Möckel is greatly acknowledged. This work was supported by grants from DFG (SFB 387), Schu 627/8-2 and BMBF 01ZZ9510/07NBL04.

## References

Abbas, C.A., Binkley, B., Surh, D.G.R. and McCaughey, G.W. (1994) "Genomic organization, exact localization, and tissue expression of the human CD26 (dipeptidyl peptidase IV) gene". *Immunogenetics* 40, 331-338.

Barclay, A.N., Birkeland, M.L., Brown, P.M., Boyers, P.A.D., Davis, P.J., Schwartz, B.C. and Williamson, J.A.F. (1993) *The Leucocyte Antigen Facts Book* (Academic Press, London).

Büding, F., Junker, U., Reinhold, D., Neubert, K., Jäger, L. and Ansorge, S. (1995) "Functional role of CD26 on human B lymphocytes". *Immunol. Lett.* 45, 47-51.

Dang, N.H., Teramoto, Y., Schlossman, S.F. und Morimoto, C. (1990) "Human helper T-cell activation: functional involvement of two distinct collagen receptors I F7 and integrin family". *J. Exp. Med.* 172, 649-652.

Darmoul, D., Leca, M., Brécault, L., Marguet, D., Sapin, C., Tricot, P., Barbat, A. and Trigano, G. (1992) "Dipeptidyl peptidase IV (CD26) gene expression in enterocyte-like colon cancer cell line HT-29 and Caco-2. Cloning of the complete human coding sequence and changes of dipeptidyl peptidase IV mRNA levels during cell differentiation". *J. Biol. Chem.* 267, 2200-2208.

David, S.J., Ikenberry, S., Wild, M.K. and van der Merwe, P.A. (1998) "CD2 and the nature of protein interactions mediating cell-cell recognition". *Immunol. Rev.* 163, 217-236.

Dunn, D., Higgins, W.E. and Wakeley, J. (1994) "Texture segmentation using 2D Gabor elementary functions". *IEEE Trans. Pattern Anal. Machine Intelligence* 16, 130-149.

Huang, R., Schneider, A., Bodo, M. and Schubert, W. (2000) "Secretion and differential localization of the proteolytic cleavage products  $\alpha$ B40 and  $\alpha$ B42 of the Alzheimer amyloid precursor protein in human fetal myogenic cells". *Eur. J. Cell. Biol.* 79, 1-7.

Hegen, M., Niedoblock, G., Klein, C.B., Stein, H. and Fleischer, B. (1990) "The T-cell triggering molecule Tp103 is associated with dipeptidyl aminopeptidase IV activity". *J. Immunol.* 144, 2908-2914.

Hegen, M., Karmoza, J., Dong, R.-P., Schlossman, S.F. and Morimoto, C. (1997) "Cross-linking of CD26 by antibody induces tyrosine phosphorylation and activation of mitogen-activated protein kinase". *Immunology* 90, 257-264.

Hedemann, G. and Ritter, H. (1999) "Combining multiple neural nets for visual feature selection and classification". *ICANN 99, Ninth International Conference on Artificial Neural Networks*, pp 365-370.

Iwata, S. and Morimoto, C. (1999) "CD26/dipeptidyl peptidase IV in context. The different roles of a ectoenzyme in malignant transformation". *J. Exp. Med.* 190, 301-306.

Kohonen, T. (1989) *Self-organization and Associative Memory* (Springer, Berlin).

Lee, T.S. (1996) "Image representation using 2d Gabor wavelets". *IEEE Trans. Pattern Anal. Machine Intelligence* 18, 959-971.

Moody, J. and Darken, C. (1989) "Fast learning in networks of locally-tuned processing units". *Neural Comput.* 1, 281-294.

Morimoto, C. and Schlossman, S.F. (1998) "The structure and function of CD26 in the T-cell immune response". *Immunol. Rev.* 161, 53-70.

Morrison, M.E., Vijayaratnam, S., Eagekar, D., Albino, A.P. and Hougham, A.N. (1993) "A marker for neoplastic progression of human melanocytes is a cell surface ectopeptidase". *J. Exp. Med.* 177, 1135-1143.

Nentkamp, T.W., Ritter, H. and Schubert, W. (1999) "Extracting patterns of lymphocyte fluorescence from digital micrographs". *Intelligent Data Analysis in Medicine and Pharmacology 99 (IDAMAP99), Workshop Notes*, Washington DC, USA, pp. 79-88.

Nentkamp, T.W., Ritter, H. and Schubert, W. (2001) "A neural classifier enabling high-throughput topological analysis of lymphocytes in tissue sections". *IEB Transaction of Information Technology in Biomedicine* 5, 138-149.

Nentkamp, T., Wenzel, H., Schubert, W. and Ritter, H. (2000b) "A neural network architecture for automatic segmentation of fluorescence micrographs". *Proceedings of the Eighth European Symposium on Artificial Neural Network (ESANN), Bruges, Belgium*.

Pigott, R. and Power, C. (1993) *The Adhesion Molecule Facts Book* (Academic Press, London).

Rao, R. and Ballard, D. (1995) "An active vision architecture based on iconic representations". Technical report, University of Rochester, CS.

Ritter, H. (1991) "Learning with the self-organizing map", In: Kohonen, T., ed, *Artificial Neural Networks I* (Elsevier Science Publishers, B.V., London).

Rummelhart, D., Hilton, G. and Williams, R. (1986) "Learning internal representations by error propagation. Parallel distributed processing: explorations in the microstructure of cognition". *Foundations* 1, 318-362.

Schubert, W. (1991) "Triple immunofluorescence confocal laser scanning microscopy: spatial correlation of novel cellular differentiation markers in human muscle biopsies". *Eur. J. Cell. Biol.* 55, 272-282.

Schubert, W. (1992) "Antigenic determinants of T-lymphocyte  $\alpha\beta$  receptor and other leukocyte surface proteins as differential markers of skeletal muscle regeneration: detection of spatially and temporally restricted pattern by MAM microscopy". *Eur. J. Cell. Biol.* 58, 395-410.

Schubert, W., Zimmermann, K., Cramer, M. and Starzinski-Powitz, A. (1989) "Lymphocyte antigen Leu-19 as a molecular marker of regeneration in human skeletal muscle". *Proc. Natl. Acad. Sci. USA* 86, 307-311.

Schubert, W., Muster, C.J. and Beyreuther, K. (1993) "APP+ T-lymphocytes selectively sorted in endoneurial tubes in polymyositis displaced NCAM-expressing muscle fibers". *Eur. J. Cell. Biol.* 62, 333-342.

Sjöstrand, P.J., Prydal, B.R. and Wohlborg, L.U. (1999) "Artificial neural network-aided image analysis system for cell counting". *Cytometry* 36, 18-26.

74

W. SCHUBERT *et al.*

Stein, H., Schwarting, R. and Niedobitek, G. (1989) In: Kapp, W., Dörken, B., Gilks, W.R., Rieber, E.P., Schmidt, R.E., Stein, H. and Kr. von dem Borne, A.B.G., eds. Leukocyte Typing IV (Oxford University Press, Oxford), pp 412-415.

Tanida, T., Camerini, D., Seedi, B., Tarimoto, Y., Dung, N.H., Kemenka, J., Dahlberg, H.N., Schlossman, S.L. and Morimoto, C. (1992) "Cloning and functional expression of the T-cell activation antigen CD 26", *J. Immunol.* 149, 481-486.

Turk, M. and Pentland, A. (1991) "Eigenfaces for recognition", *J. Cognitive Neurosci.* 3, 71-86.

Varcham, A.C.H., Rac, R. and Ritter, H. (1997) "Facial feature detection using neural networks". In: Wolfgang Gerstner, A., Germond, M.H. and Nicoud, J.-D., eds. Proceedings of the International Conference on Artificial Neural Network (Springer, Lausanne), pp 955-960.

Wahlstrom, J., Berlin, M., Skold, C.M., Wigzell, H., Eklund, A. and Grupewald, J. (1999) "Phenotypic analysis of lymphocytes and monocytes/macrophages in peripheral blood and bronchoalveolar lavage fluid from patients with pulmonary sarcoidosis". *Thorax* 54, 339-346.